RSC Advances

PAPER

View Article Online
View Journal | View Issue

Cite this: *RSC Adv.*, 2025, **15**, 3365

Facile fabrication of a novel chitosan/carboxymethyl cellulose/bentonite/CuO nanocomposite for enhanced photocatalytic and antibacterial applications†

Manisha Khandelwal,[a] Kanchan Soni,[b] Kamakhya Prakash Misra,[b] Ashima Bagaria,[b] Devendra Singh Rathore,[c] Gangotri Pemawat,[a] Ravindra Singh[d] and Rama Kanwar Khangarot *[a]

In this study, an eco-friendly chitosan/carboxymethyl cellulose/bentonite/CuO nanocomposite (CS/CMC/BN/CuO NC) was synthesized utilizing algal-mediated copper oxide nanoparticles (CuO NPs). The resulting hybrid nanocomposite was thoroughly characterized using advanced techniques, including XRD, FTIR, UV-vis, FE-SEM, HR-TEM, and BET analysis. The photocatalytic activity of the hybrid nanocomposite was assessed by the degradation of brilliant cresyl blue (BCB) dye under visible light irradiation, while the antibacterial activity of the hybrid nanocomposite was evaluated against both Gram-positive and Gram-negative bacterial strains. XRD analysis confirmed the successful synthesis of the hybrid nanocomposite (CS/CMC/BN/CuO NC) with a crystallite size of 9.66 nm. The UV-vis analysis and Tauc plot revealed that the hybrid nanocomposite exhibited an absorbance peak at 249 nm and a band gap of 2.81 eV, respectively. FE-SEM and HR-TEM analysis highlighted its unique broken-tile structure. Furthermore, the hybrid nanocomposite exhibited outstanding photocatalytic performance, achieving 98.38% degradation of BCB dye within 60 min under optimal conditions. The scavenging experiments showed that electrons (e^-) and superoxide anion radicals ($O_2^{\bullet -}$) are the major reactive species involved in the degradation of BCB dye. Additionally, it demonstrated remarkable antibacterial efficacy, showing a 40 mm zone of inhibition (ZOI) against the Gram-negative *Pseudomonas aeruginosa* strain. The findings indicate that the synthesized CS/CMC/BN/CuO NC holds significant promise for the photodegradation of organic dyes. Furthermore, it exhibits strong antibacterial properties, making it a potential disinfectant for treating wastewater contaminated with pathogenic bacteria.

Received 29th November 2024
Accepted 27th January 2025

DOI: 10.1039/d4ra08437c

rsc.li/rsc-advances

Introduction

Recent advancements in nanotechnology have facilitated the synthesis of a wide variety of nanocomposites (NCs), tailored for specific applications in fields such as electronics, medicine, energy storage, and environmental remediation.[1] NCs are materials formed by integrating nanoparticles (NPs) into a bulk matrix, resulting in unique and enhanced properties compared to their individual components. Incorporating NPs into the composite matrix can substantially enhance thermal stability, electrical conductivity, mechanical strength, and other functional properties.[2] The biopolymer-clay matrix has garnered remarkable attention globally from both academic and industrial perspectives.[3,4] The integration of biopolymer-clay matrix into metal oxide NPs significantly enhances their properties, making them suitable for various applications.[5]

Copper oxide nanoparticles (CuO NPs) provide a highly efficient and cost-effective alternative to expensive noble metals, offering comparable functionalities. Their outstanding properties impart remarkable versatility, leading to widespread use across diverse applications, including catalysis,[6] sensors,[7,8] photocatalysis,[9] and wastewater treatments.[10] Traditionally, the synthesis of CuO NPs mainly relied on chemical methods, often involving harmful chemicals and hazardous by-products. Nowadays, green synthesis methods, utilizing natural biological sources such as plants, fungi, algae, and yeast, have emerged as environmentally friendly alternatives. In our previous study, we observed that *Coelastrella terrestris* algal-

[a]*Department of Chemistry, University College of Science, Mohanlal Sukhadia University, Udaipur, 313001, Rajasthan, India. E-mail: ramakanwar@mlsu.ac.in*
[b]*Department of Physics, School of Basic Sciences, Manipal University Jaipur, Jaipur, 303007, Rajasthan, India*
[c]*Department of Environmental Sciences, Mohanlal Sukhadia University, Udaipur, 313001, Rajasthan, India*
[d]*Department of Chemistry, Maharani Shri Jaya Government Post-graduate College, Bharatpur, 321001, Rajasthan, India*

† Electronic supplementary information (ESI) available. See DOI: https://doi.org/10.1039/d4ra08437c

mediated CuO NPs displayed excellent photocatalytic and antibacterial activity.[11] The further enhancement of the properties could be achieved by combining these CuO NPs with other organic and inorganic compounds.

Chitosan (CS), a biodegradable biopolymer, possesses a wide range of biological properties. It is a natural polysaccharide consisting of β-(1 → 4)-2-amino-2-deoxy-D-glucopyranose and is formed through the deacetylation of chitin.[12] This biopolymer exhibits exceptional characteristics, such as high water permeability, non-toxicity, and biocompatibility, attributed to its amino and hydroxyl functional groups.[13] Furthermore, carboxymethyl cellulose (CMC), a derivative of cellulose, consists of glucose units linked by β-(1 → 4) glycosidic bonds. Owing to its anionic nature, CMC is water-soluble at any temperature. As one of the most extensively utilized cellulose derivatives, it finds significant applications in agriculture, medicine, and environmental sectors.[14] Additionally, bentonite (BN), mainly composed of over 75% montmorillonite, demonstrates remarkable adsorption and antibacterial properties. It is abundant in nature, cost-effective, non-toxic, and environmentally friendly. The charge imbalance present in bentonite makes it an ideal candidate for incorporating various inorganic compounds.[15,16] The synergistic combination of algal-mediated CuO NPs with CS, CMC, and BN improves the properties of the resulting nanocomposite (NC).

Therefore, this research paper presents the green synthesis of a chitosan/carboxymethyl cellulose/bentonite/CuO nanocomposite (CS/CMC/BN/CuO NC). The properties of the synthesized hybrid nanocomposite were examined using a range of characterization techniques, including X-ray diffraction (XRD), Fourier-transform infrared spectroscopy (FTIR), UV-vis spectroscopy, field-emission scanning electron microscopy (FE-SEM), high-resolution transmission electron microscopy (HR-TEM), and Brunauer–Emmett–Teller (BET) analysis. The photocatalytic activity of the hybrid nanocomposite was investigated by evaluating its ability to degrade brilliant cresyl blue (BCB) dye. Additionally, its antibacterial efficacy was evaluated against four pathogenic bacterial strains: *Staphylococcus epidermis* (*S. epidermis*), *Staphylococcus aureus* (*S. aureus*), *Escherichia coli* (*E. coli*), and *Pseudomonas aeruginosa* (*P. aeruginosa*).

Experimental section

Comprehensive details of the materials and methods utilized for the synthesis of the CS/CMC/BN/CuO NC, along with the protocols for photocatalytic experiments and antibacterial analysis, are presented in the ESI.†

Results and discussion

XRD analysis

Fig. 1 illustrates the XRD patterns of various samples, including CuO NPs, CS, CMC, BN, and the synthesized CS/CMC/BN/CuO NC. In Fig. 1(a), the diffraction peaks at 2θ values of 32.45°, 35.50°, 38.71°, and 48.81° corresponded to the (110), ($\bar{1}$11), (200), and ($\bar{2}$02) planes, respectively. These peaks, marked with triangles, are consistent with the end-centered monoclinic structure of polycrystalline CuO NPs, as per the standard JCPDS card no. 80-1916.[17] Fig. 1(b) shows the XRD pattern of CS, which exhibited diffraction peaks at 2θ values of 12.72°, 19.22°, and 26.33° (indicated by rectangles).[18–20] Fig. 1(c) disclosed the XRD pattern of CMC at 2θ peaks of 15.63°, 22.51°, and 34.52° (these peaks are marked with circles).[21] Fig. 1(d) represents the XRD pattern of BN, showing peaks at 2θ values of 19.98° and 29.86°, marked with plus signs.[16,22] Finally, Fig. 1(e) reveals the XRD pattern of the synthesized CS/CMC/BN/CuO NC. The diffraction peaks at 2θ values of 16.16°, 20.14°, 22.58°, 26.79°, 35.54°, 38.80°, and 48.89° confirm the synthesis of the hybrid nanocomposite, indicating the incorporation of CuO NPs, CS, CMC, and BN.[16,23] The distinct peaks for CS, CMC, BN, and CuO NPs are denoted by rectangles, circles, plus, and triangles, respectively, showing slight shifts in peak positions and intensities owing to the incorporation of CuO NPs within the composite matrix. The crystallite size (t_S) of synthesized NC was also evaluated using the well-known Scherrer eqn (1).[24]

$$t_S = \frac{k\lambda}{\beta\cos\theta} \quad (1)$$

$$\delta = \frac{1}{(t_S)^2} \quad (2)$$

where t_S, k, λ, β, θ, and δ denote the crystallite size of the synthesized NC, Scherrer's constant (~1), the wavelength of X-ray (0.1541 nm), full width at half maximum (FWHM) of diffraction peaks, Bragg's angle of diffraction, and dislocation density, respectively. The crystallite sizes of the synthesized CuO NPs and CS/CMC/BN/CuO NC were determined to be 7.62 nm and 9.66 nm, respectively, along their highest intensity

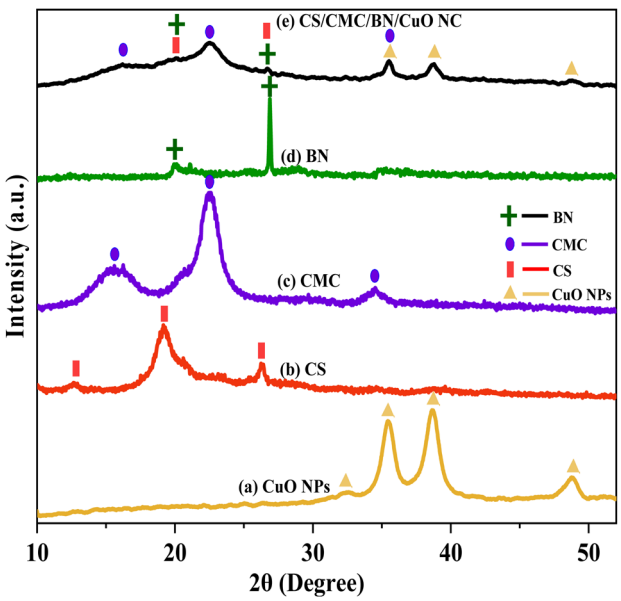

Fig. 1 XRD patterns of (a) CuO NPs, (b) chitosan (CS), (c) carboxymethyl cellulose (CMC), (d) bentonite (BN), and (e) chitosan/carboxymethyl cellulose/bentonite/CuO nanocomposite (CS/CMC/BN/CuO NC).

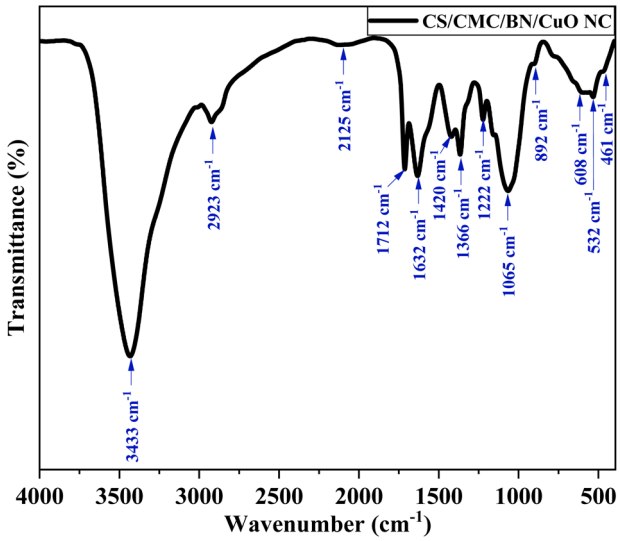

Fig. 2 FTIR spectra of synthesized CS/CMC/BN/CuO NC.

planes. Dislocation density (δ) is a critical parameter quantifying the presence of defects within crystalline solids. The dislocation density of synthesized hybrid nanocomposite was assessed using eqn (2). The dislocation density (δ) of the CuO NPs and the hybrid nanocomposite was observed to be 0.0172×10^{15} m^{-2} and 0.0107×10^{15} m^{-2}, respectively.

FTIR analysis

Fig. 2 illustrates the FTIR spectra of CS/CMC/BN/CuO NC. The FTIR spectra revealed important peaks at 3433, 2923, 2125, 1712, 1632, 1420, 1366, 1222, 1065, 892, 608, 532, and 461 cm^{-1}. The prominent peak at 3433 cm^{-1} was attributed to intermolecular hydrogen-bonded –O–H and –N–H stretching vibrations, signifying the overlap of the –O–H and –N–H peaks of CMC and CS, respectively, within the same region.[11,25] The peaks at 2923 and 1420 cm^{-1} were ascribed to the –C–H stretching and bending vibrations of alkanes, respectively, present in the CS/CMC/BN/CuO NC.[26,27] These peaks are due to metabolites present in the algal extract which act as reducing, capping, and stabilizing agents in the formation of CuO NPs.[28] The minor peak at 2125 cm^{-1} indicates the presence of –CH_3 in the hybrid nanocomposite.[25] The band at 1632 cm^{-1} was assigned to the –O–H bending vibrations and –C=O of the amide group in CS and proteins in the algal extract.[11,23] The sharp peak at 1366 cm^{-1} was ascribed to the interaction between –C–N stretching and –N–H bending vibrations of CS and algal extract. Strong peaks at 1065 and 608 cm^{-1} were ascribed to the Si–O–Si and Si–O–Al vibrations of BN.[23,29]

The peak at 892 cm^{-1} corresponded to the C–O–C stretching vibration of β-(1 → 4)-glycosidic linkages that exist in CMC.[26,30] The bands at 608, 532, and 461 cm^{-1} were associated with Cu–O stretching vibrations.[11] The FTIR spectra revealed effective interactions among CS, CMC, BN, and CuO NPs, confirming the successful formation of the CS/CMC/BN/CuO NC.

UV-vis analysis and Tauc plot

Fig. 3(a) depicts the UV-vis spectra of the synthesized CS/CMC/BN/CuO NC, which exhibit an absorption peak at 249 nm. The CS, BN, and CuO NPs show absorbance peaks around 250 nm,[31] 300 nm,[32] and 255 nm,[33] respectively. The UV-vis spectra did not display any significant peaks for CMC.[34,35] The bonding between CS, CMC, BN, and CuO NPs results in a shift in the absorption peak of synthesized NC to 249 nm. The band gap value of the synthesized hybrid nanocomposite was determined using Tauc plot, as illustrated in Fig. 3(b). The band gap (E_g) is the energy difference between a nanocomposite's valence band (VB) and conduction band (CB).[36] It is a critical factor in determining the optical and electronic properties of NC, as it influences its ability to absorb and emit light.[10] The band gap value was determined by extrapolating the linear region of the plot of $(\alpha h\nu)^2$ *versus* $h\nu$ to the *x*-axis. The observed band gap value for

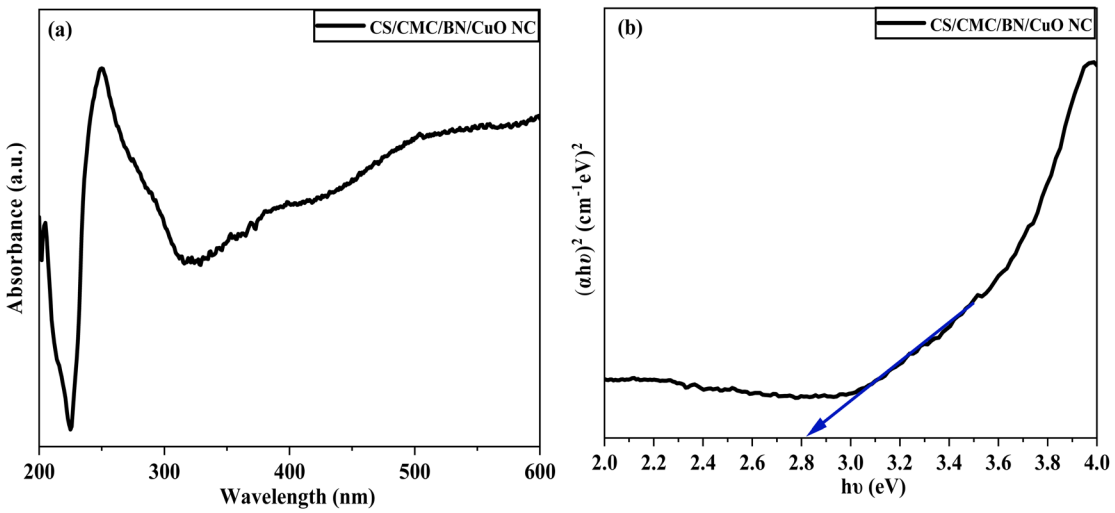

Fig. 3 (a) UV-vis spectra and (b) Tauc plot of synthesized CS/CMC/BN/CuO NC.

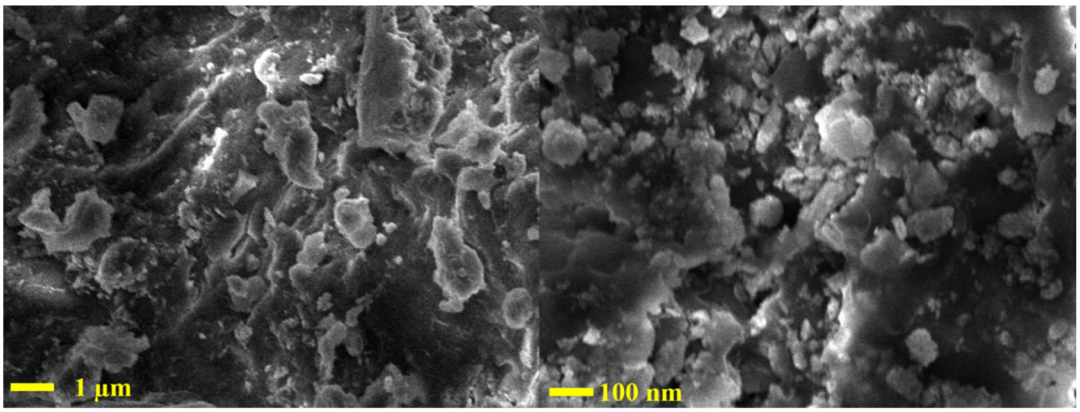

Fig. 4 FE-SEM images of CS/CMC/BN/CuO NC at different magnifications.

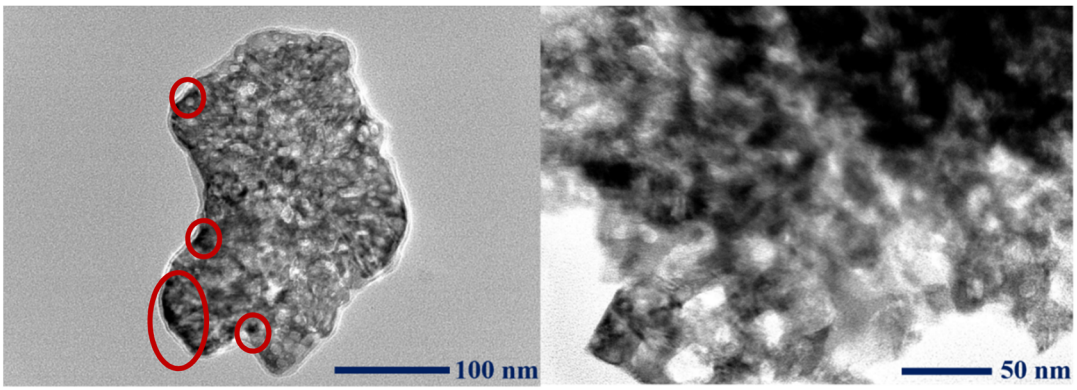

Fig. 5 HR-TEM images of CS/CMC/BN/CuO NC at different magnifications.

the synthesized CuO NPs was 2.40 eV (Fig. S1†) and for the CS/CMC/BN/CuO NC was 2.81 eV (Fig. 3(b)).

FE-SEM analysis

The morphology of synthesized CS/CMC/BN/CuO NC was analysed using FE-SEM, as shown in Fig. 4. The images indicate the formation of clusters of irregularly arranged diverse structures. The image at a 1 μm scale reveals structures resembling broken ceramic tiles. For improved clarity, a closer inspection of one structure was performed, and the broken tile-like morphology was further confirmed at a 100 nm scale. The phase segregation is not possible to observe in the obtained SEM images. Since no definite clarity on particle size or grain size could be established by FE-SEM, so we performed HR-TEM of the sample.

HR-TEM analysis

The HR-TEM analysis, presented in Fig. 5, clearly depicts the formation of a single structure composed of an aggregate of numerous fine particles. It indicates the clustering of CS/CMC/BN/CuO NC leading towards a small piece of a broken tile structure as discussed in the previous section. Hence, it can be concluded here that diverse nanostructures overlap each other contributing to the formation of the CS/CMC/BN/CuO NC. Our XRD outcomes have already established the construction of crystallites of the size 9.66 nm. Such crystallites could be noticed embedded within a single structure shown in Fig. 5. Thus, the HR-TEM findings further supports the XRD calculations concerning crystallite sizes. Furthermore, the segregated phases of CS, CMC, BN and CuO NPs are not visible in the HR-TEM. CS and BN being very small, as reflected in XRD pattern, are not visible. The broken tile structure has major content of CuO only and the second component *i.e.*, CMC which is visible at the corners/circumference in black color (under red circles).

BET analysis

Fig. 6 shows the BET analysis of the hybrid nanocomposite. Fig. 6(a) revealed a type-II adsorption–desorption isotherm, indicating multilayer adsorption on the nanocomposite. The calculated total surface area of the hybrid nanocomposite was 39.80 $m^2\ g^{-1}$. Additionally, the hybrid nanocomposite is classified as mesoporous, predominantly featuring pores with diameters ranging from 2 to 50 nm (Fig. 6(b)).

Photocatalytic degradation of BCB dye using CS/CMC/BN/CuO NC

BCB is an oxazine dye extensively utilized in the textile and printing industries, as well as a tracer in red blood cells for RNA staining (Fig. 7). BCB is recognized as a carcinogenic, toxic, and

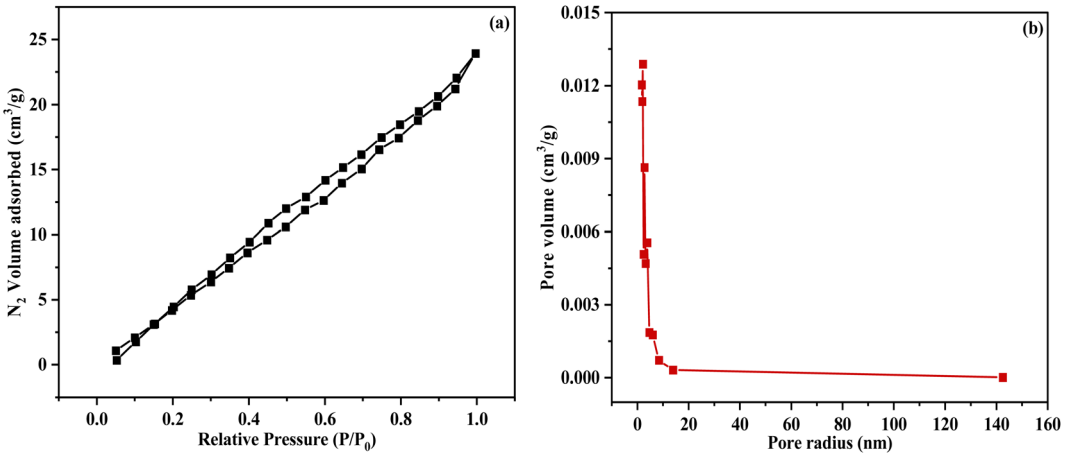

Fig. 6 (a) BET N_2 adsorption isotherm (b) Barrett–Joyner–Halenda (BJH) pore distribution.

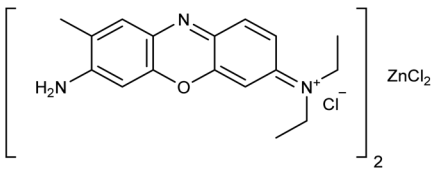

Fig. 7 Structure of BCB dye.

mutagenic compound, posing significant environmental risks even at low concentrations.[37] BCB is also used in the food industry, found in products such as ice cream, syrups, dairy products, and confectionery.[38] Its presence poses a considerable threat to aquatic ecosystems and human health, highlighting the urgent need for efficient remediation strategies.[37,39] The photocatalytic degradation of BCB dye was monitored at the maximum absorbance wavelength peak (λ_{max}) of 625 nm.[40]

The degradation of BCB dye was investigated using three processes: adsorption, photolysis, and photocatalysis (Fig. 8). This was demonstrated through two plots, Fig. 8(a) C_t/C_0 *versus* time and Fig. 8(b) degradation percentage *versus* time. In the adsorption process, CS/CMC/BN/CuO NC was used as the catalyst to degrade BCB dye in the absence of light. For the photolysis process, degradation occurred solely under light exposure without the use of a catalyst. While the photocatalysis process involved the degradation of BCB dye using both the catalyst and visible light illumination. The results indicated that after 60 min, the degradation efficiencies of BCB dye were 53.64% for adsorption, 10.62% for photolysis, and 77.51% for photocatalysis. Notably, the photocatalytic degradation using CS/CMC/BN/CuO NC demonstrated superior efficacy compared to the photolysis and adsorption. Furthermore, a series of experiments was conducted to optimize the conditions for BCB dye degradation using CS/CMC/BN/CuO NC under visible light irradiation.

Optimization of reaction parameters for the degradation of BCB dye

Effect of pH. The pH of the solution is a critical factor in the dye degradation process. Fig. 9(a) illustrates the impact of pH on the BCB dye degradation using CS/CMC/BN/CuO NC. To

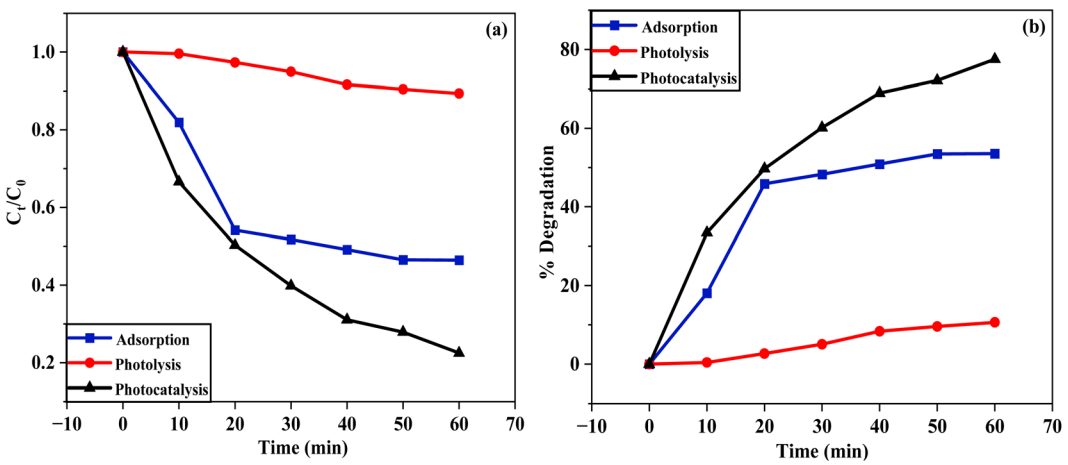

Fig. 8 Degradation of BCB dye using three processes, *i.e.*, adsorption, photolysis, and photocatalysis (a) C_t/C_0 *versus* time (b) degradation percentage *versus* time.

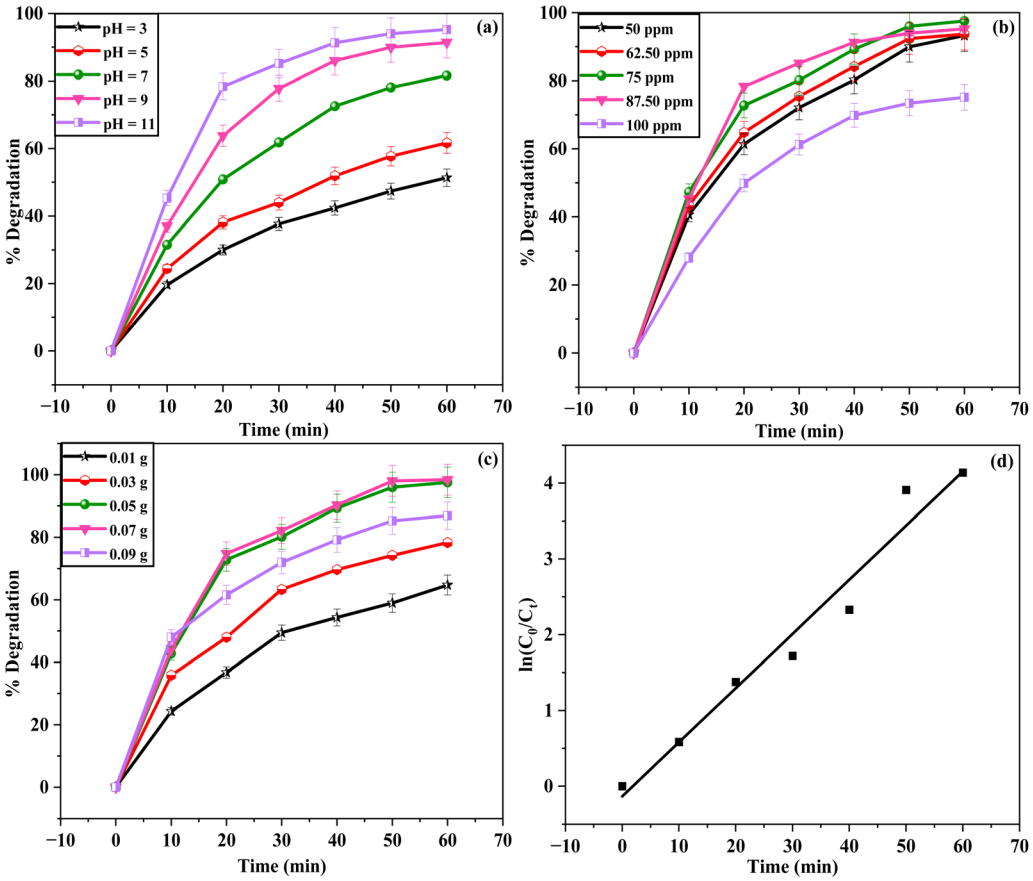

Fig. 9 Effect of (a) pH, (b) initial dye concentration, and (c) catalyst dosages on the photodegradation of BCB dye using CS/CMC/BN/CuO NC; (d) kinetic study plot of degradation of BCB dye at optimal conditions.

investigate the influence of pH on the photocatalytic degradation of BCB dye, a pH range of 3.0 to 11.0 was selected, with other parameters kept constant. The outcomes disclosed that the degradation percentages of BCB dye were 51.34%, 61.66%, 81.57%, 91.40%, and 95.24% at pH values of 3, 5, 7, 9, and 11, respectively, after 60 min of light irradiation. Notably, the degradation of BCB dye in an acidic medium was low, with degradation percentages of 51.34% at pH 3 and 61.66% at pH 5. In contrast, in a basic medium, the degradation is significantly higher, reaching 91.40% at pH 9 and 95.24% at pH 11. At a neutral pH of 7, the degradation was 81.57%.

These findings demonstrate that dye degradation increases with rising pH. In an acidic medium, the degradation of BCB dye is lower, whereas, in a basic medium, the degradation is higher. At lower pH values, the excess of H^+ ions impart a positive charge to the catalyst surface, which electrostatically repels the cationic BCB dye molecules, leading to reduced adsorption of BCB dye molecules on the surface of catalyst and lower degradation efficiency. In contrast, in a basic medium, the presence of OH^- ions results in a negative charge on the catalyst surface, enhancing the attraction of cationic BCB dye molecules, thus improving both adsorption and photodegradation efficiency. The highest degradation of 95.24% was observed at pH 11, indicating it as the optimal pH value.

Effect of initial dye concentration

The initial concentration of the dye has a significant impact on the dye degradation process. The photocatalytic efficacy of the synthesized hybrid nanocomposite was assessed at initial concentrations ranging from 50 ppm to 100 ppm at pH 11, with other parameters kept constant. Fig. 9(b) demonstrates the influence of initial dye concentration on the degradation of BCB dye using the CS/CMC/BN/CuO NC. After 60 min of visible light illumination, the degradation percentages of BCB dye were 93.24%, 93.68%, 97.53%, 95.22%, and 75.17% at initial concentrations of 50 ppm, 62.50 ppm, 75 ppm, 87.50 ppm, and 100 ppm, respectively. The degradation of BCB dye improved from 93.24% to 97.53% as the dye concentration increased from 50 ppm to 75 ppm. On the other hand, increasing the initial dye concentration from 75 ppm to 100 ppm led to a decline in the photocatalytic degradation, dropping from 97.53% to 75.17%. The maximum degradation efficiency of 97.53% was achieved at an initial dye concentration of 75 ppm. Lower degradation efficiency at lower initial dye concentrations may be due to reduced dye adsorption on the catalyst surface, leaving many active sites unoccupied. Conversely, at higher initial dye concentrations, the reduced efficacy could be due to decreased light penetration or saturation of the active sites on the catalyst surface.[11]

Table 1 Comparative photodegradation studies of BCB dye using various nanocatalysts[a]

S. no.	Nanocatalysts	Light source	Initial concentration of dye (ppm)	Catalyst dosage (mg)	pH	Time (min)	Degradation (%)	Ref.
1	Cu_2O/AA	Sunlight	50	200	7	120	73.12%	40
2	ZnO	UV	7	25	7	150	92.92%	41
3	g-C_3N_4/ZnO	Visible	25	20	10	60	99.51%	42
4	$ZnAl_2O_4$	Visible	40	1000	10	180	94.5%	43
5	ZnO/CuO	Visible	15	15	11	100	97.30%	44
6	TiO_2	UV	3	260	—	120	74%	45
7	Al_2O_3 doped Mn_3O_4	Sunlight	100	113	10	300	50–65%	46
8	Co_3O_4/Fe_2O_3	Sunlight	100	100	10	180	97%	47
9	CS/CMC/BN/CuO NC	Visible	75	70	11	60	98.38%	This work

[a] Abbreviation: AA – ascorbic acid.

These findings emphasize the importance of controlling the initial dye concentration to attain optimal efficiency in the photodegradation of dyes. The maximum BCB dye degradation of 97.53% was observed at an initial concentration of 75 ppm, leading to the selection of 75 ppm as the optimal initial concentration for BCB dye.

Effect of catalyst dosage. To assess the influence of CS/CMC/BN/CuO NC catalyst dosage on the degradation of BCB dye, the catalyst dosages were varied from 0.01 g to 0.09 g at an initial dye concentration of 75 ppm and pH 11. Fig. 9(c) shows the impact of varied catalyst dosages on BCB dye degradation. The results showed that catalyst amounts of 0.01 g, 0.03 g, 0.05 g, 0.07 g, and 0.09 g achieved degradation efficiencies of 64.71%, 78.29%, 97.53%, 98.38%, and 86.87%, respectively. The degradation enhanced from 64.71% to 98.38% as the catalyst dosage increased from 0.01 g to 0.07 g. However, increasing the catalyst dosage to 0.09 g resulted in a decreased degradation from 98.38% to 86.87%. Initially, increasing the catalyst dosage resulted in a greater number of active sites available for dye degradation, thereby enhancing degradation efficiency. However, further surges in catalyst dosage can lead to agglomeration, turbidity, and light scattering, which hinder light penetration and diminish the degradation efficiency. Consequently, the highest degradation efficacy was achieved with a catalyst dosage of 0.07 g, which was selected as the optimal dosage for BCB dye degradation. The optimal conditions for BCB dye degradation using the CS/CMC/BN/CuO NC were established as a pH of 11, an initial dye concentration of 75 ppm, and a catalyst dosage of 0.07 g.

Fig. 9(d) represents the kinetic plot of $\ln(C_0/C_t)$ *versus* time under these optimized conditions. The kinetic data were well-described by the pseudo-first-order kinetic model, suggesting that the degradation process follows pseudo-first-order kinetics. The calculated kinetic rate constant (k) and R^2 values for the photodegradation of BCB dye in the presence of CS/CMC/BN/CuO NC were found to be 0.07149 min^{-1} and 0.96712, respectively. Table 1 represents a comparative analysis of the photocatalytic degradation of BCB dye using various nanocatalysts.

Reusability of the hybrid nanocomposite

The practical applicability of the synthesized hybrid nanocomposite for photodegradation is evidenced by its photostability and reusability. To evaluate this, experiments were conducted to assess the photocatalytic degradation of BCB dye using the CS/CMC/BN/CuO NC over four consecutive cycles under visible light illumination (Fig. 10). After each cycle, the photocatalyst was recovered *via* centrifugation, washed with deionized (DI) water and ethyl alcohol, and dried in an oven at 70 °C for 4 h prior to reuse in the subsequent cycle. Fig. 10 indicates that a slight decrease in the %degradation was observed after each successive cycle. The degradation

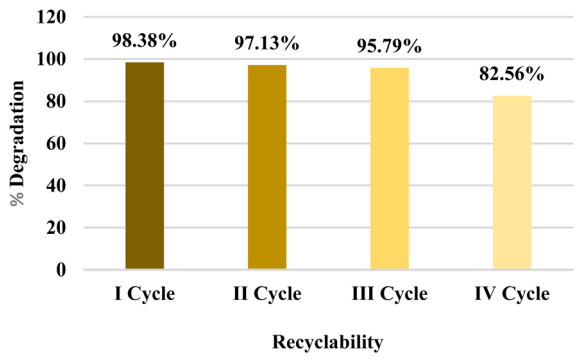

Fig. 10 Reusability of the CS/CMC/BN/CuO NC for the photodegradation of BCB dye.

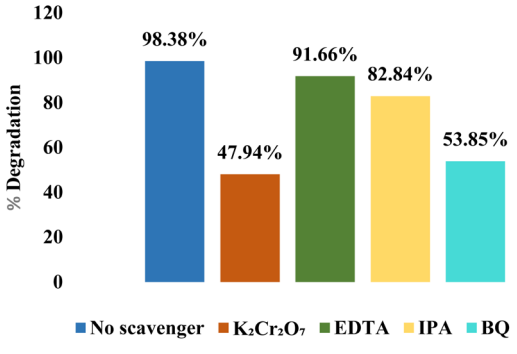

Fig. 11 Effect of specific scavengers on the photodegradation of BCB dye using CS/CMC/BN/CuO NC.

percentage declined from 98.38% to 82.56% after four successive cycles.

These findings indicate that the synthesized hybrid nanocomposite exhibits remarkable stability and reusability for BCB dye degradation. The reduction in photocatalytic activity observed after repeated cycles can be ascribed to two primary factors. First, the recollection process may lead to a loss of photocatalyst, reducing the amount of active catalyst and its efficiency. Second, intermediate species generated during the dye degradation process may deposit on the active sites of the catalyst, resulting in reduced photocatalytic activity.

Scavenging activity. The primary reactive species involved in the degradation process were identified through the reactive species trapping experiments. These experiments targeted specific reactive species, including holes (h^+), electrons (e^-), superoxide anion radicals ($O_2^{\bullet -}$), and hydroxyl radicals ($^{\bullet}OH$), using ethylenediaminetetraacetic acid (EDTA), potassium dichromate ($K_2Cr_2O_7$), benzoquinone (BQ), and isopropyl alcohol (IPA), respectively. The results, depicted in Fig. 11, highlight the contribution of each reactive species to the overall degradation process. The control experiment, without a scavenger, showed the highest degradation rate of 98.38%. The addition of $K_2Cr_2O_7$, EDTA, IPA, and BQ reduced the degradation percentages of BCB dye to 47.94%, 91.66%, 82.84%, and 53.85%, respectively. The significant reduction in degradation efficacy to 47.94% with $K_2Cr_2O_7$ and 53.85% with BQ indicates that electrons (e^-) and superoxide anion radicals ($O_2^{\bullet -}$) are the major reactive species involved in the degradation of BCB dye. The addition of IPA reduced the degradation percentage to 82.84%, suggesting that $^{\bullet}OH$ play a minor role in the degradation process. In contrast, the addition of EDTA did not noticeably reduce the degradation percentage (91.66%), indicating that holes (h^+) do not directly participate in the degradation process but contribute to the generation of other reactive species. These results provide important insights into the mechanistic pathways involved in the photocatalytic degradation process of BCB dye using CS/CMC/BN/CuO NC.

A plausible mechanism for photodegradation

The mechanism for the photodegradation of BCB dye of a hybrid nanocomposite was elucidated through scavenging experiments and band gap analysis, as depicted in Fig. 12 and also shown by eqn (3)–(8). When CS/CMC/BN/CuO NC was exposed to visible light irradiation, electrons (e^-) were excited from the VB to the CB, resulting in the generation of electron (e^-)–hole (h^+) pairs. The incorporation of CS, CMC, and BN significantly enhances the adsorption capacity and porosity of the catalyst, facilitating the adsorption of BCB dye molecules onto the catalyst surface. This high affinity and porous structure enable efficient migration of dye molecules from the solution to the catalyst surface. CS, CMC, and BN also play a vital role in preventing the recombination of electron (e^-)–hole (h^+) pairs, thereby enhancing the efficiency of CS/CMC/BN/CuO NC in the photodegradation of BCB dye.

The improved separation of electron (e^-)–hole (h^+) increases the availability of these charge carriers for successive reactions with other species, facilitating the formation of ROS critical for dye degradation. As illustrated in eqn (6) and (7), these reactive species react with water (H_2O) and oxygen (O_2) molecules, producing superoxide anion ($O_2^{\bullet -}$) and hydroxyl ($^{\bullet}OH$) radicals. These radicals serve as highly effective oxidants that promote the oxidation of BCB dye molecules, ultimately converting them into inorganic acids, water, and carbon dioxide.[40,42,44] After degradation, the adsorption sites on the hybrid nanocomposite are regenerated, allowing for its recyclable use.

Antimicrobial activity of synthesized CS/CMC/BN/CuO NC

The hybrid nanocomposite (CS/CMC/BN/CuO NC) disclosed outstanding antibacterial activity against all test pathogens, as

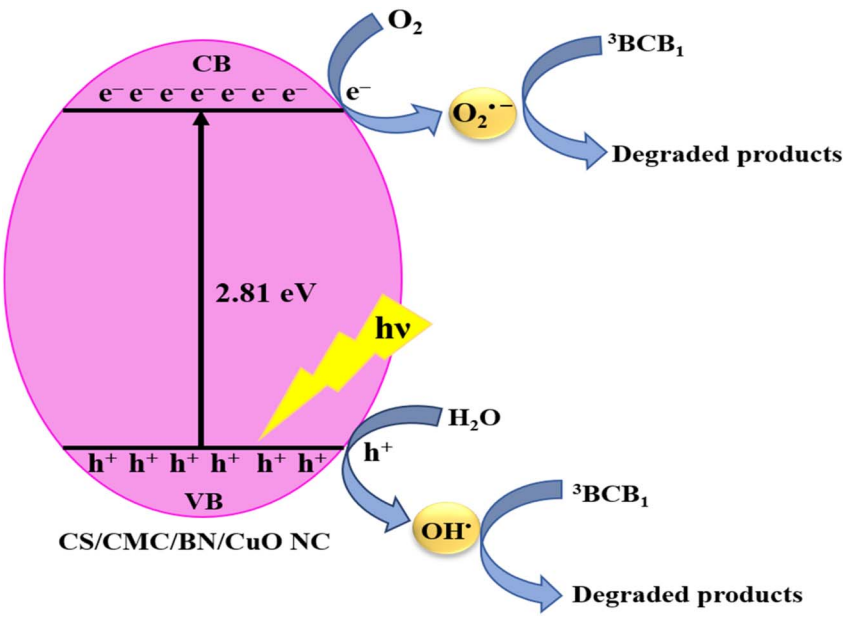

Fig. 12 A plausible mechanism of the photodegradation of BCB dye using hybrid nanocomposite (CS/CMC/BN/CuO NC).

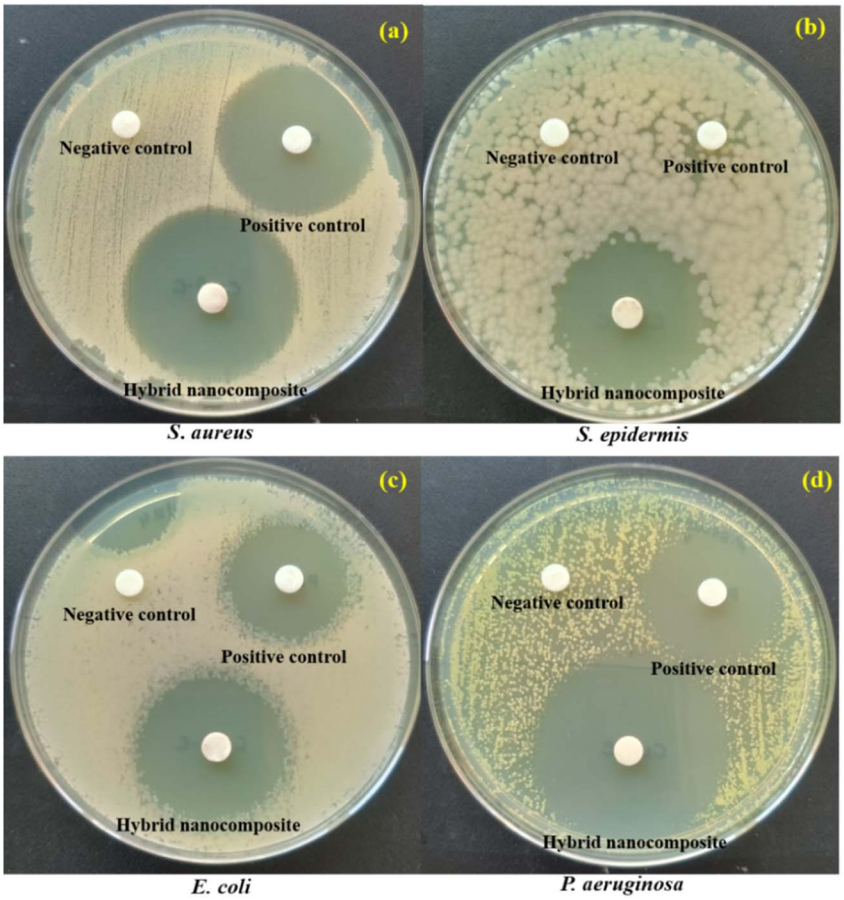

Fig. 13 Antibacterial activity of negative control, positive control, and hybrid nanocomposite against four test pathogens (a) *S. aureus*, (b) *S. epidermis*, (c) *E. coli*, and (d) *P. aeruginosa*.

Table 2 ZOI (mm) of negative control, positive control, and hybrid nanocomposite against four test pathogens[a]

		Zone of inhibition (mm)		
S. no.	Pathogens	Negative control	Positive control	Hybrid nanocomposite
1	*S. aureus*	NA	26 mm	30 mm
2	*S. epidermis*	NA	Non countable	29 mm
3	*E. coli*	NA	30 mm	35 mm
4	*P. aeruginosa*	NA	29 mm	40 mm

[a] Abbreviation: NA – not applicable.

illustrated in Fig. 13 and Table 2. Erythromycin was employed as the positive control (antibiotic), whereas DI water was utilized as the negative control in the antibacterial analysis. The calculated ZOI for *S. aureus*, *S. epidermis*, *E. coli*, and *P. aeruginosa* were 30 mm, 29 mm, 35 mm, and 40 mm, respectively. For a better comparison of antibacterial activity, a bar graph is also represented (Fig. 14). The higher ZOI values were shown by the hybrid nanocomposite than the positive control for all pathogenic bacteria. The hybrid nanocomposite showed the highest antibacterial activity against *P. aeruginosa* (Gram-negative bacteria) with a ZOI value of 40 mm and the lowest against *S. epidermis* (Gram-positive bacteria) with a ZOI value of 29 mm. The *S. epidermis* bacterial strain showed non-countable ZOI using positive control while synthesized hybrid nanocomposite displayed 29 mm of ZOI value. Therefore, the synthesized hybrid nanocomposite can used as an efficient antibacterial agent for the *S. epidermis* which is resistant to erythromycin antibiotic. The hybrid nanocomposite showed higher ZOI values against Gram-negative bacterial strains, *E. coli* and *P. aeruginosa*, compared to Gram-positive bacterial strains, *S. aureus* and *S. epidermis*. This difference in antimicrobial activity is likely due to the distinct structural components of Gram-

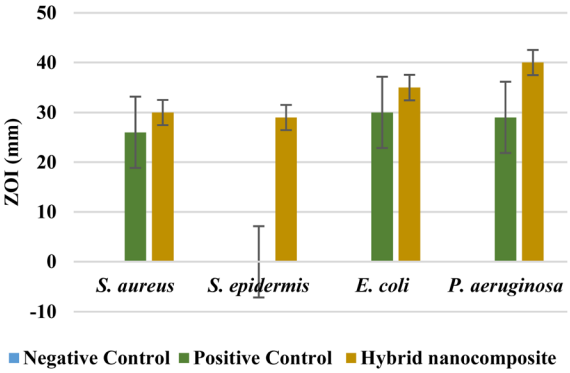

Fig. 14 Antibacterial activity of negative control, positive control, and hybrid nanocomposite (CS/CMC/BN/CuO NC) against four test pathogens; *S. aureus*, *S. epidermis*, *E. coli*, and *P. aeruginosa*.

negative and Gram-positive bacteria. Gram-negative bacteria have a thin peptidoglycan layer covered by an outer membrane composed of lipopolysaccharides. In contrast, the Gram-positive bacteria possess a thicker peptidoglycan layer.

$$^{1}BCB_0 \xrightarrow{h\nu} {}^{1}BCB_1 \quad (3)$$

$$^{1}BCB_1 \xrightarrow{ISC} {}^{3}BCB_1 \quad (4)$$

$$CS/CMC/BN/CuO\ NC \xrightarrow{h\nu} CS/CMC/BN/CuO\ NC\ (e_{CB}^{-} + h_{VB}^{+}) \quad (5)$$

$$h_{VB}^{+} + H_2O \rightarrow {}^{\bullet}OH + H^{+} \quad (6)$$

$$O_2(\text{dissolved oxygen}) + e_{CB}^{-} \rightarrow O_2^{\bullet -} \quad (7)$$

$$^{3}BCB_1 + e_{CB}^{-} + O_2^{\bullet -} + {}^{\bullet}OH \rightarrow \text{degraded products} \quad (8)$$

The synthesized hybrid nanocomposite interacts with amino acids and carbohydrate components found in the peptidoglycan layer. Gram-negative bacteria, characterized by a thinner peptidoglycan layer, are more susceptible to damage by the hybrid nanocomposite, while Gram-positive bacteria, possessing a thicker peptidoglycan layer, exhibit greater resistance to its effects. Furthermore, components present in the lipopolysaccharide layer of Gram-negative bacteria enhance the negative charge on the cell membrane which can increase the susceptibility of Gram-negative bacteria towards the hybrid nanocomposite.[48,49] Our earlier research indicated that CuO NPs synthesized using *Coelastrella terrestris* algae exhibited notable antibacterial activity, showing a zone of inhibition (ZOI) of 22 mm against *S. aureus* and 17 mm against *P. aeruginosa*.[11] While the hybrid nanocomposite synthesized in this research displayed superior antibacterial efficacy, with ZOI values of 30 mm for *S. aureus* and 40 mm for *P. aeruginosa*. Table 3 represents a comparative analysis of the antibacterial activity of various previously reported NCs/NPs. The data clearly demonstrates that the synthesized hybrid nanocomposite (CS/CMC/BN/CuO NC) exhibits significantly enhanced antibacterial efficacy compared to the other NCs/NPs studied. This highlights the superior potential of the synthesized hybrid nanocomposite in antibacterial applications.

FE-SEM analysis of antibacterial activity

The FE-SEM images of pathogenic bacteria before and after exposure to the hybrid nanocomposite are shown in Fig. 15. The FE-SEM analysis disclosed that the pathogens treated with a hybrid nanocomposite exhibited substantial deformation and damage to the bacterial cellular structure, whereas the untreated (control) bacterial samples showed an intact cellular structure. In this study, exposure of the hybrid nanocomposite to *S. aureus*, *S. epidermidis*, *E. coli*, and *P. aeruginosa* resulted in

Table 3 Comparative analysis of antibacterial activity of some previously reported nanocomposites/nanoparticles[a]

S. no.	Nanocomposites/nanoparticles (NCs/NPs)	Target bacteria	ZOI (mm)	References
1	CuO NPs	*S. aureus*	22	11
		P. aeruginosa	17	
2	CS-CuO NC	*S. aureus*	~5	50
		E. coli	~9	
3	CS-CUR-GO/CuO hybrid nanocomposite	*S. aureus*	~12.4	
		E. coli	~16	
4	CS-CuO NC	*S. aureus*	13	51
		E. coli	10	
5	CS-CuO NPs	*S. aureus*	17 ± 1.54	52
		E. coli	24 ± 1.99	
		P. aeruginosa	23 ± 1.88	
6	CMC/CuO NC	*S. aureus*	19	53
		E. coli	14	
7	CS/CMC/BN/CuO NC	*S. aureus*	30	This work
		S. epidermis	29	
		E. coli	35	
		P. aeruginosa	40	

[a] Abbreviation: CUR – curcumin, GO – graphene oxide.

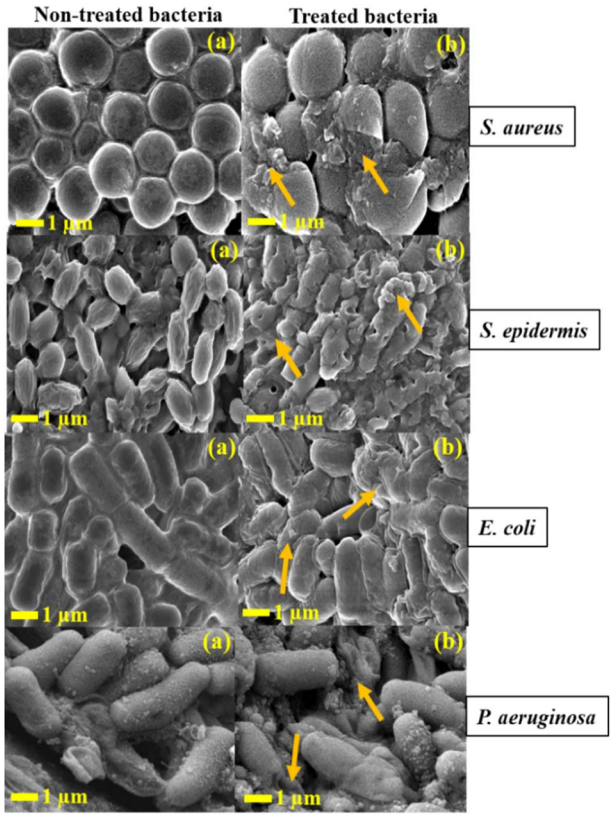

Fig. 15 FE-SEM images of (a) all non-treated samples represent control and (b) all treated samples with hybrid nanocomposite. The arrows indicate rupture of the cell membrane.

noticeable malformation of the bacterial cell membrane. The bacterial cell membrane is crucial for maintaining electrical potential difference of the bacterial cell. Untreated bacterial strains display an electrical potential difference of ~100–200 mV. There is higher negative potential outside the cell and lower negative potential inside the cell. Therefore, the hybrid nanocomposite accumulates on the negatively charged bacterial cell membrane and binds to it and reducing the potential difference. This interaction induces membrane depolarization, resulting in membrane leakiness. Eventually, cell rupture occurs when the potential difference of cell reaches zero.[54,55]

A plausible mechanism for the antibacterial activity

The hybrid nanocomposite (CS/CMC/BN/CuO NC) demonstrates exceptional antibacterial activity due to the synergistic effects of the CS/CMC/BN matrix and algal-mediated CuO NPs. The CS/CMC/BN matrix increased the surface area of the hybrid nanocomposite thereby enhancing the antibacterial activity of CuO NPs by promoting greater adsorption of the hybrid nanocomposite onto bacterial surfaces. CS, a natural biopolymer, exhibits notable antibacterial properties. The positively charged amino groups of CS can readily bind to the negatively charged bacterial cell surfaces, disrupting normal cell membrane functions. Intracellularly, CS penetrates the bacterial nuclei and binds with DNA, inhibiting the synthesis of mRNA and proteins.[56] The incorporation of CMC with CuO NPs enhances the dispersity and stability of CuO NPs in solution, thus improving the antibacterial activity of CuO NPs.[57]

Additionally, the inclusion of BN increases the surface area and avoids aggregation of the hybrid nanocomposite.[58,59] The plausible mechanism of antibacterial activity of synthesized hybrid nanocomposite (CS/CMC/BN/CuO NC) is illustrated in Fig. 16. FE-SEM analysis revealed that treatment of the hybrid nanocomposite with bacteria resulted in the rupture of pathogenic bacterial cell membranes, leading to the leakage of cellular components such as plasmids, ribosomes, and cytoplasm. The small size of the nanocomposite enables it to penetrate the cell membrane, interact with intracellular components, and inhibit the synthesis of mRNA and proteins in

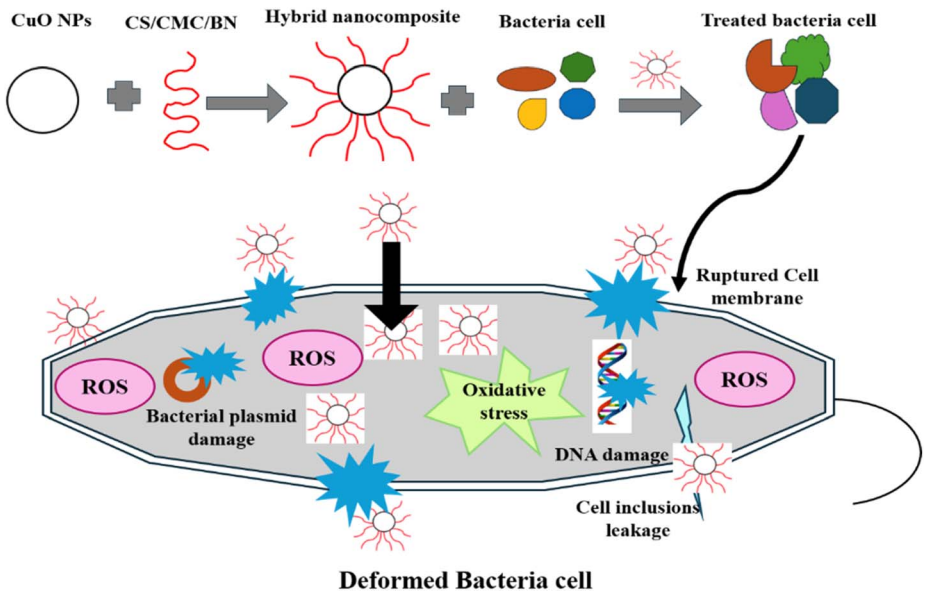

Fig. 16 Schematic illustration of the antibacterial activity mechanism of hybrid nanocomposite (CS/CMC/BN/CuO NC).

DNA. Furthermore, this interaction also generates ROS, causing oxidative damage to organelles, leading to damage of lipid, protein, and DNA.[11,55,60]

Conclusions

The present study demonstrates the synthesis of hybrid nanocomposite (CS/CMC/BN/CuO NC) using a biogenic route. The synthesized hybrid nanocomposite was characterized by techniques such as XRD, UV-Vis, FTIR, FE-SEM, and HR-TEM. The XRD analysis disclosed a crystallite size of 9.66 nm for the hybrid nanocomposite along the highest intensity plane. FE-SEM and HR-TEM images depicted a broken tile structure of the hybrid nanocomposite. Further, both XRD and FTIR analysis confirmed the incorporation of the CS/CMC/BN matrix with CuO NPs. The hybrid nanocomposite disclosed excellent photocatalytic activity in the degradation of BCB dye, achieving a maximum degradation percentage of 98.38% at pH 11, with a catalyst dosage of 0.07 g and an initial dye concentration of 75 ppm after 60 min. The kinetics of the photodegradation reaction followed pseudo-first-order kinetics, with a kinetic rate constant (k) of 0.07149 min^{-1}. The hybrid nanocomposite exhibited the highest antibacterial activity against *P. aeruginosa* with a ZOI value of 40 mm and the lowest antibacterial activity against *S. epidermis* with a ZOI value of 29 mm. The synthesized hybrid nanocomposite demonstrated exceptional photocatalytic and antibacterial activity, making it a promising candidate for environmental and biological applications.

Data availability

The data supporting this article have been included as part of the ESI.†

Author contributions

Manisha Khandelwal: investigation, visualization, data curation, formal analysis, methodology, writing – original draft. Kanchan Soni: investigation, data curation, methodology. Kamakhya Prakash Misra: formal analysis, resources, validation, writing – review & editing. Ashima Bagaria: resources, validation. Devendra Singh Rathore: software, resources, validation. Gangotri Pemawat: software, resources. Ravindra Singh: software, resources. Rama Kanwar Khangarot: conceptualization, visualization, methodology, resources, supervision, validation, writing – review & editing.

Conflicts of interest

There are no conflicts to declare.

Acknowledgements

R. K. K. and M. K. thank the University Grants Commission, New Delhi, India, for the UGC-Start-Up Project [No. F. 30-476/2019 (BSR)] and Fellowship [115/CSIRNETJUNE2019], respectively, for providing financial support to conduct the research work. DSR thanks the Science and Engineering Research Board, Department of Science and Technology (DST), New Delhi, for a core research grant (CRG/2019/006919). The authors thank the Department of Chemistry, Mohanlal Sukhadia University, Udaipur (Raj.), India, for providing the necessary laboratory facilities. The authors are grateful to the Department of Physics, Department of Botany, and Department of Environmental Science, Mohanlal Sukhadia University, Udaipur, for providing the XRD facility, algal culture, and photocatalytic activity, respectively. The authors are grateful to MNIT Jaipur for UV-vis and BET analysis and Punjab University for HR-TEM analysis. The authors acknowledge the facilities of Manipal University Jaipur (MUJ), India, for FE-SEM and antibacterial analysis.

References

1 P. Nguyen-Tri, T. A. Nguyen, P. Carriere and C. Ngo Xuan, *Int. J. Corros.*, 2018, **2018**, 4749501.
2 W. S. Khan, N. N. Hamadneh and W. A. Khan, in *Science and Applications of Tailored Nanostructures*, 2016, pp. 50–67.
3 F. Z. Zeggai, F. Touahra, R. Labied, D. Lerari, R. Chebout and K. Bachari, in *Biopolymers-clay Nanocomposites: Synthesis Pathways, Properties, and Applications*, IntechOpen, 2024.
4 J.-W. Rhim and Y.-T. Kim, in *Innovations in Food Packaging*, Elsevier, 2014, pp. 413–442.
5 M. Nozari, M. Gholizadeh, F. Zahiri Oghani and K. Tahvildari, *Int. J. Biol. Macromol.*, 2021, **184**, 235–249.
6 M. A. Bhosale, S. C. Karekar and B. M. Bhanage, *ChemistrySelect*, 2016, **1**, 6297–6307.
7 R. K. Khangarot, M. Khandelwal and R. Singh, in *Metal Nanocomposites for Energy and Environmental Applications*, Springer, 2022, pp. 489–508.
8 S. Steinhauer, *Chemosensors*, 2021, **9**, 51.
9 K. ur Rehman, A. Ullah Khan, K. Tahir, S. Nazir, K. Albalawi, H. M. A. Hassan, E. A. Alabbad, M. S. Refat, H. S. Al-Shehri and A. Mohammed Aldawsari, *J. Mol. Liq.*, 2022, **360**, 119453.
10 M. Khandelwal, S. Choudhary, A. Kumawat, K. P. Misra, D. S. Rathore and R. K. Khangarot, *RSC Adv.*, 2023, **13**, 28179–28196.
11 M. Khandelwal, S. Choudhary, Harish, A. Kumawat, K. P. Misra, Y. Vyas, B. Singh, D. S. Rathore, K. Soni and A. Bagaria, *Int. J. Nanomed.*, 2024, 4137–4162.
12 S. Sathiyavimal, V. Seerangaraj, T. Kaliannan and A. Pugazhendhi, *Carbohydr. Polym.*, 2020, **241**, 116243.
13 P. S. Umoren, D. Kavaz, A. Nzila, S. S. Sankaran and S. A. Umoren, *Polymers*, 2022, **14**, 1832.
14 S. S. Salem, A. H. Hashem, A.-A. M. Sallam, A. S. Doghish, A. A. Al-Askar, A. A. Arishi and A. M. Shehabeldine, *Polymers*, 2022, **14**, 3352.
15 J. Li, Suyoulema, W. Wang and Sarina, *Solid State Sci.*, 2009, **11**, 2037–2043.
16 B. Krishnan and S. Mahalingam, *Adv. Powder Technol.*, 2017, **28**, 2265–2280.
17 S. Asbrink and A. Waskowska, *J. Phys. Condens. Matter*, 1991, **3**, 8173.
18 D. Bharathi, R. Ranjithkumar, B. Chandarshekar and V. Bhuvaneshwari, *Int. J. Biol. Macromol.*, 2019, **129**, 989–996.

19 D. Bharathi, R. Ranjithkumar, B. Chandarshekar and V. Bhuvaneshwari, *Int. J. Biol. Macromol.*, 2019, **141**, 476–483.
20 S. Sathiyavimal, S. Vasantharaj, T. Kaliannan and A. Pugazhendhi, *Carbohydr. Polym.*, 2020, 116243.
21 J. L. Sharma, V. Dhayal and R. K. Sharma, *3 Biotech*, 2021, **11**, 269.
22 M. Khatamian, B. Divband and R. Shahi, *J. Water Process. Eng.*, 2019, **31**, 100870.
23 K. Kaur, Khushbu, V. Vaid, Anupama, Anshul, Ankush and R. Jindal, *Polym. Bull.*, 2023, **80**, 6609–6634.
24 M. Khandelwal, A. Kumawat, K. P. Misra and R. K. Khangarot, *Part. Sci. Technol.*, 2022, **41**, 640–652.
25 K. D. Khalil, S. M. Riyadh, S. M. Gomha and I. Ali, *Int. J. Biol. Macromol.*, 2019, **130**, 928–937.
26 I. M. Araújo, R. R. Silva, G. Pacheco, W. R. Lustri, A. Tercjak, J. Gutierrez, J. R. Júnior, F. H. Azevedo, G. S. Figuêredo and M. L. Vega, *Carbohydr. Polym.*, 2018, **179**, 341–349.
27 Z. A. Raza, A. Mobeen, M. S. U. Rehman and M. I. Majeed, *Polym. Bull.*, 2023, **80**, 11031–11047.
28 D. O. B. Apriandanu and Y. Yulizar, *Mater. Lett.*, 2021, **284**, 128911.
29 M. Honarmand, M. Golmohammadi and A. Naeimi, *Mater. Chem. Phys.*, 2020, **241**, 122416.
30 D. Ciolacu, F. Ciolacu and V. I. Popa, *Cellul. Chem. Technol.*, 2011, **45**, 13.
31 V. Thamilarasan, V. Sethuraman, K. Gopinath, C. Balalakshmi, M. Govindarajan, R. A. Mothana, N. A. Siddiqui, J. M. Khaled and G. Benelli, *J. Clust. Sci.*, 2018, **29**, 375–384.
32 N. Venkatathri, *Bull. Catal. Soc. India*, 2006, **5**, 61–72.
33 M. H. Sarfraz, M. Zubair, B. Aslam, A. Ashraf, M. H. Siddique, S. Hayat, J. N. Cruz, S. Muzammil, M. Khurshid and M. F. Sarfraz, *Front. Microbiol.*, 2023, **14**, 1188743.
34 G. Li, L. Liu, Y. Sun and H. Liu, *J. Clust. Sci.*, 2018, **29**, 1193–1199.
35 L. Mansouri, S. Benghanem, M. Elkolli and B. Mahmoud, *Polym. Bull.*, 2020, **77**, 85–105.
36 H. M. Alhusaiki Alghamdi, *Opt. Mater.*, 2022, **134**, 113101.
37 E. Cako, K. D. Gunasekaran, R. D. Cheshmeh Soltani and G. Boczkaj, *Water Resour. Ind.*, 2020, **24**, 100134.
38 J. L. Tinoco, L. F. Muñoz Villegas, V. I. Y. Sánchez, F. A. N. Perez and J. M. Z. Rodriguez, *MRS Adv.*, 2024, **9**, 283–288.
39 B. Mandal and S. K. Ray, *J. Taiwan Inst. Chem. Eng.*, 2016, **60**, 313–327.
40 S. Zeghdi, S. E. Laouini, H. A. Mohammed, A. Bouafia, M. L. Tedjani, M. M. S. Abdullah and T. Trzepieciński, *Materials*, 2024, **17**, 2358.
41 R. Messai, M. F. Ferhat, B. Belmekki, M. W. Alam, M. A. S. Al-Othoum and S. Sadaf, *Mater. Res. Express*, 2024, **11**, 015006.
42 P. L. Meena, K. Poswal, A. K. Surela and J. K. Saini, *Adv. Compos. Hybrid Mater.*, 2023, **6**, 16.
43 A. A. Abd-Allah, Y. M. Ahmed, S. M. El-Sheikh, A. O. Youssef and A. M. Amin, *J. Water Environ. Nanotechnol.*, 2022, **7**, 288–305.
44 P. L. Meena, A. K. Surela and K. Poswal, *J. Water Environ. Nanotechnol.*, 2021, **6**, 196–211.
45 P. Singh, M. MAbdullah, S. Sagadevan, C. Kaur and S. Ikram, *Optik*, 2019, **182**, 512–518.
46 S. A. B. Asif, S. B. Khan and A. M. Asiri, *Nanoscale Res. Lett.*, 2015, **10**, 355.
47 S. A. B. Asif, S. B. Khan and A. M. Asiri, *Nanoscale Res. Lett.*, 2014, **9**, 510.
48 G. Applerot, J. Lellouche, A. Lipovsky, Y. Nitzan, R. Lubart, A. Gedanken and E. Banin, *Small*, 2012, **8**, 3326–3337.
49 D. Franco, G. Calabrese, S. P. Guglielmino and S. Conoci, *Microorganisms*, 2022, **10**, 1778.
50 A. Sanmugam, L. K. Sellappan, A. Sridharan, S. Manoharan, A. B. Sairam, A. I. Almansour, S. Veerasundaram, H.-S. Kim and D. Vikraman, *Antibiotics*, 2024, **13**, 620.
51 S. B. Ahmed, H. I. Mohamed, A. M. Al-Subaie, A. I. Al-Ohali and N. M. R. Mahmoud, *Sci. Rep.*, 2021, **11**, 9540.
52 M. H. Sarfraz, S. Muzammil, S. Hayat, M. Khurshid and A. H. Sayyid, *Int. J. Biol. Macromol.*, 2023, **242**, 124954.
53 M. Yadollahi, I. Gholamali, H. Namazi and M. Aghazadeh, *Int. J. Biol. Macromol.*, 2015, **73**, 109–114.
54 K. Soni and A. Bagaria, *J. Exp. Mar. Biol. Ecol.*, 2024, **577**, 152026.
55 D. Mitra, E.-T. Kang and K. G. Neoh, *ACS Appl. Mater. Interfaces*, 2019, **12**, 21159–21182.
56 N. Rezazadeh and A. Kianvash, *J. Appl. Polym. Sci.*, 2021, **138**, 50552.
57 C. Huang, M. Xiao, H. Cui, J. Wang, Y. Cai and Y. Ke, *Int. J. Biol. Macromol.*, 2023, **252**, 126495.
58 A. Mokhtar, A. B. Ahmed, B. Asli, B. Boukoussa, M. Hachemaoui, M. Sassi and M. Abboud, *Minerals*, 2023, **13**, 1268.
59 S. C. Motshekga, S. S. Ray, M. S. Onyango and M. N. B. Momba, *J. Hazard. Mater.*, 2013, **262**, 439–446.
60 X. Ma, S. Zhou, X. Xu and Q. Du, *Front. Surg.*, 2022, **9**, 905892.